

LETTERS

Demonstration of high-responsivity epitaxial β - Ga_2O_3 /GaN metal–heterojunction–metal broadband UV-A/UV-C detector

To cite this article: Anisha Kalra *et al* 2018 *Appl. Phys. Express* **11** 064101

View the [article online](#) for updates and enhancements.

You may also like

- [ConvGRU-MHM: a CNN GRU-enhanced MHM for mitigating GNSS multipath](#)
Runfa Tong, Chao Liu, Yuan Tao *et al.*
- [High-Performance Metal Hard Mask Process Using Fiber-Textured TiN Film for Cu Interconnects](#)
Naoki Torazawa, Takeshi Harada, Tatsuya Kabe *et al.*
- [Metal hydride hydrogen compressors for energy storage systems: layout features and results of long-term tests](#)
Boris P Tarasov, Mikhail S Bocharnikov, Yurii B Yanenko *et al.*

Demonstration of high-responsivity epitaxial β -Ga₂O₃/GaN metal–heterojunction–metal broadband UV-A/UV-C detector

Anisha Kalra[†], Sandeep Vura[†], Shashwat Rathkanthiwar, Rangarajan Muralidharan, Srinivasan Raghavan, and Digbijoy N. Nath

Center for Nano Science and Engineering, Indian Institute of Science, Bangalore, 560012, India

[†]These authors contributed equally to this work.

Received March 22, 2018; accepted April 9, 2018; published online April 27, 2018

We demonstrate epitaxial β -Ga₂O₃/GaN-based vertical metal–heterojunction–metal (MHM) broadband UV-A/UV-C photodetectors with high responsivity (3.7 A/W) at 256 and 365 nm, UV-to-visible rejection $>10^3$, and a photo-to-dark current ratio of ~ 100 . A small (large) conduction (valence) band offset at the heterojunction of pulsed laser deposition (PLD)-grown β -Ga₂O₃ on metal organic chemical vapor deposition (MOCVD)-grown GaN-on-silicon with epitaxial registry, as confirmed by X-ray diffraction (XRD) azimuthal scanning, is exploited to realize detectors with an asymmetric photoresponse and is explained with one-dimensional (1D) band diagram simulations. The demonstrated novel vertical MHM detectors on silicon are fully scalable and promising for enabling focal plane arrays for broadband ultraviolet sensing.

© 2018 The Japan Society of Applied Physics

Solar-blind photodetectors operating in the ultraviolet (UV) region of the electromagnetic spectrum have a wide range of astronomical, strategic, and terrestrial applications, particularly those that require devices to be insensitive to the visible and infrared (IR) clutter within the atmosphere.^{1,2)} Several applications, including dosimetry during UV phototherapy, flame detection, bio-aerosol detection, non-destructive forensic examination, and astronomical imaging, require detectors with a broadband UV spectral response.^{3,4)} Although wide-band-gap semiconductors such as III–nitrides (Al_xGa_{1-x}N) and emerging β -Ga₂O₃ are attractive candidates for high-efficiency UV photodetectors owing to their intrinsic solar blind nature, achieving a broadband or multi-spectral UV sensor is still a major challenge. This is because the spectral response reaches a peak near the band edge and falls off gradually (sharply) on the short (long)-wavelength side of the peak.

A broadband UV detector is theoretically possible using heterojunctions of Al_xGa_{1-x}N and GaN by exploiting the tunable band gap and enabling selective wavelength absorption in a vertical device topology. However, material challenges, such as cracking of thick Al_xGa_{1-x}N layers on GaN as a result of severe lattice mismatch, and a high conduction band discontinuity (ΔE_C) at the Al_xGa_{1-x}N/GaN interface⁵⁾ have held back the development of such multi-spectral UV sensors. In particular, the large ΔE_C impedes the flow of photo-generated electrons in a vertical device geometry, even if GaN is grown on Al_xGa_{1-x}N to circumvent the cracking issue in a possible back-illuminated approach. Although p–i–n-based heterostructures with multiple blocking layers of AlGaN with various Al mole fractions have been utilized to realize multi-spectral detectors, wavelength tunability is restricted owing to growth complexity.³⁾ While the emerging β -Ga₂O₃ devices are heralding a new dawn of microelectronics^{6,7)} and optoelectronics^{8–12)} thanks to their many advantages over rival wide-band-gap competitors,¹³⁾ the study of (Al_xGa_{1-x})₂O₃ alloys for possible band gap tailoring towards broadband UV sensing is yet to reach even an embryonic stage.

We demonstrate a broadband UV-A/UV-C detector formed by energy band engineering of an epitaxial β -Ga₂O₃/GaN stack on a silicon (111) platform. The detectors, with a high spectral responsivity of 3.7 A/W and a good visible rejection exceeding three orders of magnitude at an applied bias of 5 V,

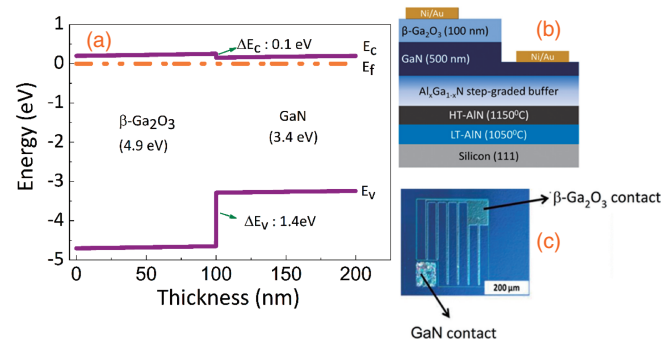


Fig. 1. (a) Equilibrium energy band diagram of the β -Ga₂O₃/GaN heterojunction simulated using a one dimensional Schrodinger–Poisson solver software BandEng. (b) Schematic of the device epi-stack showing β -Ga₂O₃ and GaN as the active absorption layers. (c) Optical micrograph of the fabricated device.

provide a band-pass response between ~ 256 and 365 nm by utilizing both β -Ga₂O₃ and GaN as the active absorption layers in the detector architecture and exploiting the small $\Delta E_C \sim 0.1$ eV at the Ga₂O₃/GaN interface [Fig. 1(a)].^{14,15)} Such a broadband response is not feasible by any III–nitride-only or (Al_xGa_{1-x})₂O₃-only heterostructures. In fact, epitaxial heterojunctions of III–nitrides/(Al_xGa_{1-x})₂O₃, which are promising for enabling next-generation high-performance transistors and optoelectronic devices via physical and functional integration, are little investigated. Most of the existing reports on β -Ga₂O₃/GaN photodetectors are based on either lateral metal–semiconductor–metal (MSM) detectors fabricated on polycrystalline β -Ga₂O₃ films realized through thermal oxidation of GaN^{16–18)} or on device architectures wherein the built-in electric field across the n- β -Ga₂O₃/p-GaN junction depletion region has been utilized for the separation of photogenerated carriers.^{19,20)} In addition, the detector epi-stacks are grown on sapphire in all these cases. Owing to the silicon platform, a vertical device architecture, and lower growth complexity owing to the absence of doped layers, the metal–heterojunction–metal (MHM) detectors reported in this letter are fully scalable and can easily enable focal plane arrays (FPAs) for multi-spectral/broadband UV sensing.

The schematic of the device epi-stack is shown in Fig. 1(b). High-crystalline-quality 500-nm-thick GaN epi-layers were grown on (111) silicon in an Aixtron 200/4-HT horizontal-

flow low-pressure metal organic chemical vapor deposition (MOCVD) reactor. Prior to growth, the silicon wafer was cleaned ex situ as well as in situ, as described by Chandrasekar et al.²¹⁾ The growth began with a two-step AlN layer (a 60 nm layer grown at 1050 °C followed by a 90 nm layer grown at 1150 °C), that, along with a micron-thick AlGaN step-graded buffer, helped realize a GaN layer with a very smooth surface morphology (<1 nm rms roughness over a 10 × 10 μm² scan area) and low surface pit density. Subsequently, pulsed laser deposition (PLD) was used to grow a 100-nm-thick β-Ga₂O₃ film. 99.99%-purity Sigma-Aldrich Ga₂O₃ crystalline powder was pressed and sintered at 1300 °C for 10 h to prepare the target. The deposition chamber was evacuated to 5 × 10⁻⁶ mbar, after which the substrate was heated to 700 °C by resistive heating. Prior to deposition, the target was precleaned using 1000 laser pulses at a fluence of 2 J/cm² and repetition frequency of 5 Hz. During deposition, the fluence was maintained at 2 J/cm² and the target was rotated at a speed of 2–3 rpm. After the deposition, samples were cooled to room temperature in vacuum. The crystallinity and structural quality of the deposited films were investigated using a Rigaku four-circle X-ray diffractometer.

Vertical MHM photodetector devices [Fig. 1(c)] with an active device area of 0.1 mm² were realized using i-line optical lithography-based patterning for top (Ga₂O₃) and bottom (GaN) layers. The mesa region was defined by reactive ion etching (RIE) of the Ga₂O₃ layer using a Cl₂/BCl₃/Ar-based gas chemistry, and the etch depth was confirmed to be ~300 nm from atomic force microscopy-based step-height measurements. E-beam-evaporated Ni/Au (30/100 nm) was used to form Schottky contacts to both active layers.

The details of photocurrent and spectral responsivity measurements are reported elsewhere.²²⁾ A Schrödinger–Poisson solver along with standard material parameters was used for the band diagram simulations.^{23,24)}

The X-ray diffraction (XRD) θ – 2θ scan [Fig. 2(a)] of the epi-stack shows the Bragg reflections corresponding to β-Ga₂O₃, wurtzite GaN, and silicon. The peaks at 2θ values of 18.90, 38.32, and 59.18° correspond to the (201) family of planes of β-Ga₂O₃. The Bragg reflections at 34.53 and 36.11° correspond to (002) planes of GaN and AlN, respectively, whereas those at 34.88, 35.19, and 35.56° (marked by the symbol ♣) emerge from the step-graded AlGaN-buffer layers beneath the GaN absorber layer. The peaks at 28.31 and 58.74° correspond to the (111) and (222) planes of Si, respectively. Thus, from the θ – 2θ scan, it can be confirmed that β-Ga₂O₃ is phase pure and is oriented such that (201)_{Ga2O3} || (002)_{GaN} || (111)_{Si}. The ϕ -scans shown in Fig. 2(b) further confirm the in-plane orientation of β-Ga₂O₃ with respect to GaN. Six peaks separated by 60° confirmed the six-fold symmetry for both GaN(110) and β-Ga₂O₃(111). Since β-Ga₂O₃ has a monoclinic structure, the {111} planes exhibit two-fold rotation symmetry, but the underlying GaN surface exhibits threefold rotational symmetry leading to the growth of three crystallographic variants along each direction at the same rate, resulting in six-fold rotational symmetry in the ϕ -scans.^{25,26)} From θ – 2θ and ϕ -scans we can determine the orientational relationships to be (201)_{Ga2O3} || (001)_{GaN}, [102]_{Ga2O3} || [100]_{GaN}, [010]_{Ga2O3} || [110]_{GaN}, [102]_{Ga2O3} || [110]_{GaN}, and [102]_{Ga2O3} || [100]_{GaN}. Full width at half maximum (FWHM) values of the XRD rocking curves (ω -scans) of symmetric and asymmetric planes

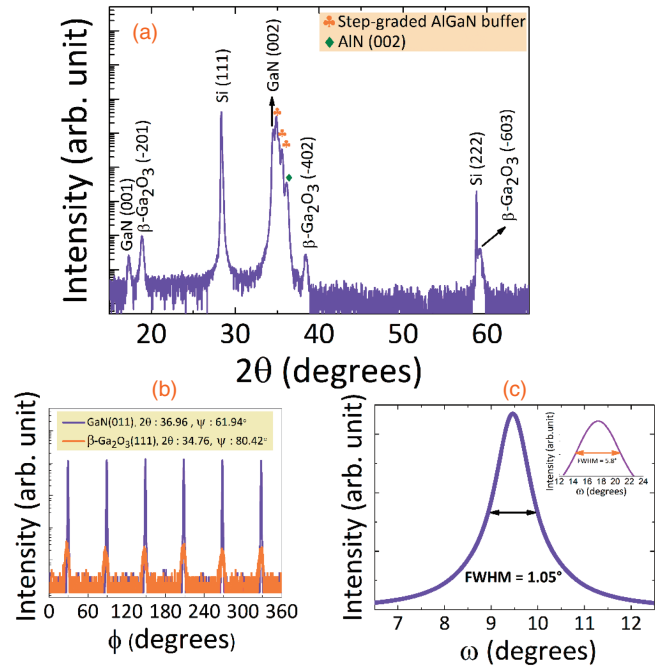


Fig. 2. (a) High-resolution XRD θ – 2θ scan confirming the (201) epitaxial registry of monoclinic β-Ga₂O₃ on (001) GaN. (b) Six peaks in the ϕ -scans of (011) plane of GaN and (111) plane of β-Ga₂O₃ confirming the out-of-plane orientation. (c) ω scans of the symmetric (201) and asymmetric (111) planes (inset) of monoclinic β-Ga₂O₃.

Table I. FWHM values (deg) of rocking curves of symmetric and asymmetric planes of GaN and β-Ga₂O₃.

GaN(002)	GaN(102)	β-Ga ₂ O ₃ (201)	β-Ga ₂ O ₃ (111)
0.24	0.40	1.05	5.80

for GaN and β-Ga₂O₃ [Fig. 2(c)] are compiled in Table I. The typical background carrier concentrations in the grown Ga₂O₃ and GaN layers are ~10¹⁵ cm⁻³, as determined by contactless Hall and resistivity measurements.

For the discussion that follows, the measurement configuration where the MHM devices are biased such that Ga₂O₃ is biased positive with respect to GaN will be termed forward bias and that where Ga₂O₃ is biased negative with respect to GaN, reverse bias. The current–voltage (I – V) characteristics across the devices under dark and UV illumination (at 256 and 365 nm, corresponding to β-Ga₂O₃ and GaN band edges, respectively) were then investigated for the two different bias conditions. Asymmetry is observed between the dark (I_{Dark}) and light (I_{Light}) current levels under different bias conditions (Fig. 3). The dark current across the detectors is always limited by the current across the reverse-biased Schottky contact and hence, the dark current is limited by the current across the reverse-biased Ni/GaN Schottky barrier under forward bias and by the current across the Ni/Ga₂O₃ barrier under reverse bias. The marginally higher Schottky barrier height for the Ni/Ga₂O₃ junction compared to the Ni/GaN junction^{27,28)} explains the small asymmetry in the dark I – V characteristics. The optical power density of the xenon lamp used for these measurements was 6.7 mW/cm² at 256 nm and 20.1 mW/cm² at 365 nm illumination wavelengths, which explains the lower measured light current at 256 nm than that at 365 nm under both bias conditions. The ratio of the currents measured under UV and dark illumination, however, exceeds

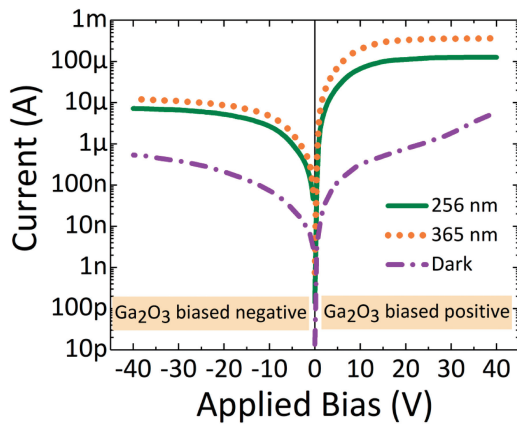


Fig. 3. I - V characteristics (semilog scale) showing the asymmetry in the dark and light currents measured across the fabricated detectors under the two different bias configurations. The lower light current at 256 nm than that at 365 nm is due to a lower power emitted by the xenon lamp at 256 nm (6.7 mW/cm^2) than that at 365 nm (20.1 mW/cm^2).

two orders of magnitude at all bias voltages. The asymmetry with respect to the bias direction is, nevertheless, more pronounced for light current than for dark current, which can be attributed to the band alignment at the heterojunction. Under illumination, the photogenerated holes drift towards the Ni/GaN contact under forward bias, whereas under reverse bias, they drift towards the Ni/Ga₂O₃ contact. The asymmetry in the forward and reverse I - V characteristics for light current (at both 365 and 256 nm) could be attributed to the fact that holes (in GaN) face a large valence band offset (1.4 eV) at the GaN/Ga₂O₃ interface while drifting to the Ni/Ga₂O₃ contact under reverse bias, unlike under forward bias conditions. Thus, the number of holes reaching the Ni/GaN contact (i.e., forward bias) is much larger than the number reaching the Ni/Ga₂O₃ contact (under reverse bias). Moreover, there could also be a difference in the degree of hole trapping at the two contacts. This, along with the possible large difference in the number of holes reaching the two electrodes (and therefore, asymmetric barrier lowering), leads to asymmetric I - V characteristics under forward and reverse biases.

Spectral responsivity (SR) values at any given values of applied bias and wavelength were calculated by obtaining the ratio of the measured photocurrent ($I_{\text{Photo}} = I_{\text{Light}} - I_{\text{Dark}}$) with the optical power (P_{op}) at that wavelength. The variation of SR with wavelength for different values of applied bias is shown in Figs. 4(a) and 4(b). When Ga₂O₃ is biased positive with respect to GaN, the device exhibits a broadband UV-A/UV-C spectral response with peaks at wavelengths corresponding to the band gap of the two absorption layers (256 and 365 nm), with a high DC spectral responsivity of 3.7 A/W at both 256 and 365 nm for an applied bias of 5 V. The broadband spectral responsivity exceeded 25 A/W at an applied bias of 40 V and the dark-current-limited near zero-bias detectivity for these detectors was estimated to be $4.7 \times 10^{10} \text{ cm Hz}^{1/2} \text{ W}^{-1}$. The measured external quantum efficiency (EQE) exceeds 100%, indicating an internal gain mechanism in these devices. We have previously reported the observation of similar gain mechanisms in Al(GaN)²² and Ga₂O₃¹¹ MSM lateral photodetectors, and our experiments revealed trapping of photogenerated holes by negatively charged acceptor states present either at the metal/semi-

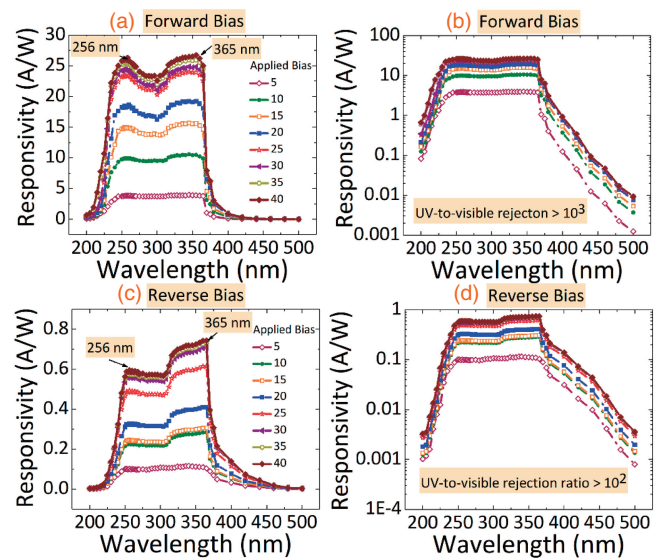


Fig. 4. SR variation with wavelength under (a, b) forward and (c, d) reverse bias.

conductor interface or in the semiconductor bulk with a consequent barrier lowering under UV illumination to be a plausible reason for the same. A similar hole-trapping associated photo-induced barrier lowering might be contributing to the observed gain and consequently a high responsivity (or EQE) in the case of these MHM detectors as well. Under the reverse-bias conditions, the response at 365 nm is enhanced compared with that at 256 nm: 0.6 and 0.75 A/W at 256 and 365 nm, respectively, at 40 V. The UV-to-visible rejection ratio, which is defined as the ratio of the SR at 500 nm to that at 365 nm, exceeded three orders of magnitude under both bias conditions.

To confirm that the observed spectral response at 256 nm included a contribution from photogeneration in the β -Ga₂O₃ epi-layer and was not due to low-wavelength (high-energy) absorption in GaN, the spectral response measured across devices with similar geometry fabricated on the GaN-only region (a small portion intentionally masked during Ga₂O₃ growth) in the same wafer was compared with the response obtained for MHM detectors at the same bias voltage (5 V in this case). The SR for the devices on the GaN layer reached a peak at 365 nm (3.3 A/W) and fell on both the higher- and lower-wavelength sides of that peak (Fig. 5) without any peak at 256 nm, which is in contrast to the UV (256 nm)-enhanced spectral response for the β -Ga₂O₃/GaN MHM devices. This confirms the β -Ga₂O₃-based origin of the observed high SR (3.7 A/W) at 256 nm for the MHM detectors, and the measured responsivity values compare well with the ones reported in the literature for β -Ga₂O₃-based detectors.^{11,26,29–30} The relatively sharp fall in responsivity for sub-365 nm wavelengths across the GaN-only detectors is not observed for the MHM detectors, which can be attributed to a reduced surface recombination velocity at the GaN surface in the case of the MHM detectors, suggesting that Ga₂O₃ acts as an efficient surface passivation layer for GaN. Therefore, the broadband spectral response is due to absorption and photogeneration in GaN and Ga₂O₃ as well as to the passivation effect of crystalline Ga₂O₃ in enhancing the sub-365 nm response of GaN, leading to a high response between the two peaks, i.e., between 256 and 365 nm. It should, however, be noted that

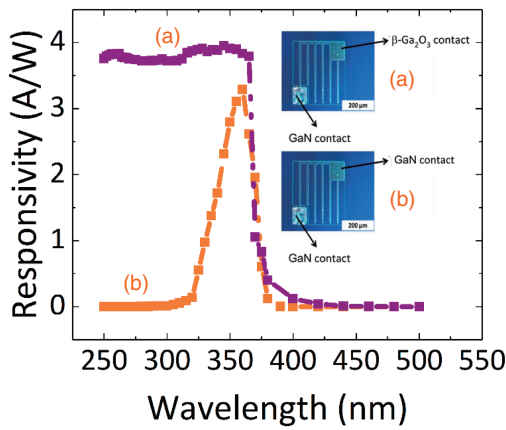


Fig. 5. SR variation with wavelength at applied bias of 5 V for similar geometry detectors fabricated on (a) β -Ga₂O₃/GaN heterojunction and (b) GaN to confirm the β -Ga₂O₃-based origin of the 256 nm band edge for the MHM device.

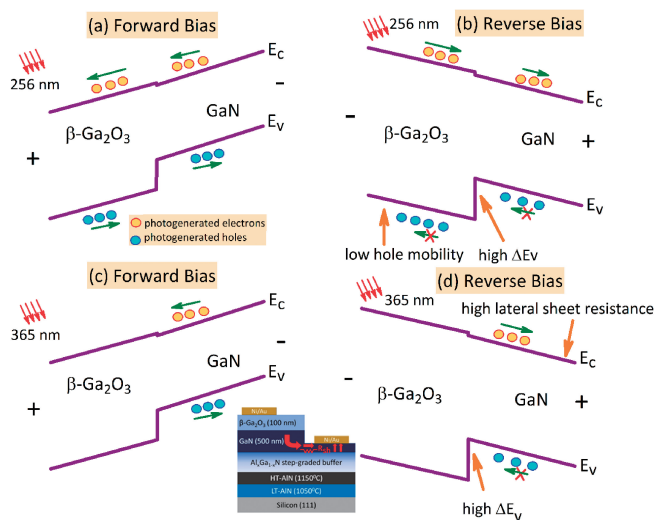


Fig. 6. Energy band diagrams of the β -Ga₂O₃/GaN heterointerface under various bias configurations and illumination conditions to explain the observed device characteristics.

the passivation layer alone cannot contribute to a distinct band edge^{31–33} at 256 nm and that the band edge at 256 nm observed for these detectors is indeed contributed to by the collection of photogenerated carriers in the Ga₂O₃ layer.

The asymmetry in the obtained spectral response with respect to the bias conditions can be explained using the energy band diagrams shown in Fig. 6. Under forward bias and 256 nm illumination [Fig. 6(a)], ~63% of the light will be absorbed in the 100-nm-thick Ga₂O₃ (assuming an absorption coefficient of 10⁵ cm⁻¹),³⁴ and photocarriers will be generated in Ga₂O₃ as well as in GaN. The low conduction band offset at the heterointerface allows photo-generated electrons in GaN to get collected at the positively biased Ga₂O₃ contact. Photo-generated holes in GaN get collected at the negatively biased GaN electrode. The high hole effective mass and the consequent low hole mobility²⁴ in the Ga₂O₃ layer do not allow the collection of photo-generated holes at the negatively biased GaN contact, and the major contribution to photocurrent under 256 nm illumination is by electron collection at the Ga₂O₃ contact. Under reverse bias [Fig. 6(b)], photo-generated holes in GaN cannot get collected because of the

high valence band offset at the heterointerface. The photo-generated electrons however, get collected at the positively biased GaN electrode. Under 365 nm illumination [Figs. 6(c) and 6(d)], carriers will be generated only in the GaN layer since the top Ga₂O₃ is transparent to this wavelength. These carriers will be efficiently collected under forward bias but will face a high lateral sheet resistance during reverse bias. By lateral sheet resistance, we are referring to the resistance associated with the lateral flow of electrons in GaN as they get collected at the Ni/GaN junction (indicated by the red arrow in the schematic of the epi-stack in Fig. 6). Under reverse bias, as illustrated in the band diagram schematic, the photo-generated electrons in GaN must travel a lateral path of about 3 μ m to accumulate at the Ni contact. However, for forward bias, the field direction is the opposite, and the photogenerated electrons are swept to the Ni/Ga₂O₃ contact where the carriers need to travel only a vertical distance of approximately 300 nm. This is what leads to the observed reduced spectral responsivity under reverse bias. The higher SR at 365 nm than that at 256 nm for the reverse-biased configuration possibly arises from the fact that carriers generated in the β -Ga₂O₃ epi-layer must traverse a greater distance than those generated in the GaN layer. This can lead to them becoming trapped/recombined before they can get collected at the positive GaN electrode.

Improved crystalline quality of the epi-layers and the interface between them, along with sidewall passivation, contact annealing, and a smoother etched surface morphology, can help mitigate the relatively high dark current. In addition, device design modifications, such as doping the underlying GaN n-type layer, replacing the Schottky GaN contact with an ohmic contact, and the use of a thicker β -Ga₂O₃ layer, could enable a self-powered dual-band UV-A/UV-C photodetector in this MHM architecture.

In summary, we demonstrated a vertical metal–heterojunction–metal photodetector that utilizes the epitaxial integration of the two most promising candidates for UV photodetection, β -Ga₂O₃ and GaN, on a silicon (111) platform. The devices exhibited a broadband spectral response in the 256 to 365 nm wavelength region with a responsivity of 3.7 A/W at 5 V. A UV-to-visible rejection ratio exceeding three orders of magnitude and a near-zero-bias dark-current-limited detectivity of 4.7 \times 10¹⁰ cm Hz^{1/2} W⁻¹ were observed for the detectors. This device design circumvents the need for doping or an ohmic contact, and the vertical topology allows the integration of these detectors into arrays that can be utilized for UV-imaging applications.

Acknowledgments This research was supported by Joint Advanced Technology Program (JATP), grant number JATP0152, and by the Department of Science and Technology (DST) under its Water Technology Initiative (WTI), grant number DST01519. The authors would like to acknowledge support from the Research and Development work undertaken under the Ph.D. scheme of Media Lab Asia, Ministry of Electronics and Information Technology (MeitY). We would also like to thank the Micro and Nano Characterization Facility (MNCF) and National Nano Fabrication Centre (NNfC) staff at CeNSE, IISc for their help and support in carrying out this work.

- 1) M. P. Ulmer, M. Razeghi, and E. Bigan, *Proc. SPIE* **2397**, 210 (1995).
- 2) M. Razeghi and A. Rogalski, *J. Appl. Phys.* **79**, 7433 (1996).
- 3) S. Aslam, L. Miko, C. Stahle, D. Franz, D. Pugel, B. Guan, J. P. Zhang, and R. Gaska, *Electron. Lett.* **43**, 1382 (2007).
- 4) G. A. Shaw, A. M. Siegel, J. Model, A. Geboff, S. Soloviev, A. Vert, and P. Sandvik, *Proc. SPIE* **7320**, 73200J (2009).

- 5) V. Palankovski and R. Quay, *Analysis and Simulation of Heterostructure Devices* (Springer, New York, 2004) p. 63.
- 6) M. Higashiwaki, K. Sasaki, H. Murakami, Y. Kumagai, A. Koukitu, A. Kuramata, T. Masui, and S. Yamakoshi, *Semicond. Sci. Technol.* **31**, 034001 (2016).
- 7) J. Yang, S. Ahn, F. Ren, S. J. Pearton, S. Jang, and A. Kuramata, *IEEE Electron Device Lett.* **38**, 906 (2017).
- 8) Q. Feng, L. Huang, G. Han, F. Li, X. Li, L. Fang, X. Xing, J. Zhang, W. Mu, Z. Jia, D. Guo, W. Tang, X. Tao, and Y. Hao, *IEEE Trans. Electron Devices* **63**, 3578 (2016).
- 9) M. Zhong, Z. Wei, X. Meng, F. Wu, and J. Li, *J. Alloys Compd.* **619**, 572 (2015).
- 10) D. Guo, Z. Wu, P. Li, Y. An, H. Liu, X. Guo, H. Yan, G. Wang, C. Sun, L. Li, and W. Tang, *Opt. Mater. Express* **4**, 1067 (2014).
- 11) A. S. Pratiyush, S. Krishnamoorthy, S. V. Solanke, Z. Xia, R. Muralidharan, S. Rajan, and D. N. Nath, *Appl. Phys. Lett.* **110**, 221107 (2017).
- 12) P. Jaiswal, U. U. Muazzam, A. S. Pratiyush, N. Mohan, S. Raghavan, R. Muralidharan, S. A. Shivashankar, and D. N. Nath, *Appl. Phys. Lett.* **112**, 021105 (2018).
- 13) S. J. Pearton, J. Yang, P. H. Cary, F. Ren, J. Kim, M. J. Tadjer, and M. A. Mastro, *Appl. Phys. Rev.* **5**, 011301 (2018).
- 14) W. Wei, Z. Qin, S. Fan, Z. Li, K. Shi, Q. Zhu, and G. Zhang, *Nano Lett.* **7**, 562 (2012).
- 15) E. G. Villora, K. Shimamura, K. Kitamura, K. Aoki, and T. Ujiie, *Appl. Phys. Lett.* **90**, 234102 (2007).
- 16) W. Y. Weng, T. J. Hsueh, S. J. Chang, G. J. Huang, and H. T. Hsueh, *IEEE Sens. J.* **11**, 999 (2011).
- 17) Z. D. Huang, W. Y. Weng, S. J. Chang, C. J. Chiu, T. J. Hsueh, and S. L. Wu, *IEEE Sens. J.* **13**, 3462 (2013).
- 18) Z. D. Huang, W. Y. Weng, S. J. Chang, Y. F. Hua, C. J. Chiu, and T. Y. Tsai, *IEEE Photonics Technol. Lett.* **25**, 1809 (2013).
- 19) S. Nakagomi, T. Sato, Y. Takahashi, and Y. Kokubun, *Sens. Actuators A* **232**, 208 (2015).
- 20) P. Li, H. Shi, K. Chen, D. Guo, W. Cui, Y. Zhi, S. Wang, Z. Wu, Z. Chen, and W. Tang, *J. Mater. Chem. C* **5**, 10562 (2017).
- 21) H. Chandrasekar, N. Mohan, A. Bardhan, K. N. Bhat, N. Bhat, N. Ravishankar, and S. Raghavan, *Appl. Phys. Lett.* **103**, 211902 (2013).
- 22) S. Rathkantiwar, A. Kalra, S. V. Solanke, N. Mohta, R. Muralidharan, S. Raghavan, and D. N. Nath, *J. Appl. Phys.* **121**, 164502 (2017).
- 23) M. Grundmann, BandEng [<http://my.ece.ucsb.edu/mgrundmann/bandeng/>].
- 24) S. I. Stepanov, V. I. Nikolaev, V. E. Bougrov, and A. E. Romanov, *Rev. Adv. Mater. Sci.* **44**, 63 (2016).
- 25) F. B. Zhang, K. Saito, T. Tanaka, M. Nishio, and Q. X. Guo, *J. Cryst. Growth* **387**, 96 (2014).
- 26) T. Oshima, T. Okuno, and S. Fujita, *Jpn. J. Appl. Phys.* **46**, 7217 (2007).
- 27) Y. Yao, R. Gangireddy, J. Kim, K. K. Das, R. F. Davis, and L. M. Porter, *J. Vac. Sci. Technol. B* **35**, 03D113 (2017).
- 28) D. Qiao, L. S. Yu, S. S. Lau, J. M. Redwing, J. Y. Lin, and H. X. Jiang, *J. Appl. Phys.* **87**, 801 (2000).
- 29) T. Oshima, T. Okuno, N. Arai, N. Suzuki, S. Ohira, and S. Fujita, *Appl. Phys. Express* **1**, 011202 (2008).
- 30) D.-S. Wu, S.-L. Ou, R.-H. Horng, P. Ravadgar, T.-Y. Wang, and H.-Y. Lee, *Proc. SPIE* **8263**, 826317 (2012).
- 31) M.-L. Lee, T. S. Mue, F. W. Huang, J. H. Yang, and J. K. Sheu, *Opt. Express* **19**, 12658 (2011).
- 32) H.-Y. Liu, Y.-H. Wang, and W.-C. Hsu, *IEEE Sens. J.* **15**, 5202 (2015).
- 33) P.-C. Chang, C.-H. Chen, S.-J. Chang, Y.-K. Su, C.-L. Yu, B.-R. Huang, and P.-C. Chen, *Thin Solid Films* **498**, 133 (2006).
- 34) F. Ricci, F. Boschi, A. Baraldi, A. Filippetti, M. Higashiwaki, A. Kuramata, V. Fiorentini, and R. Fornari, *J. Phys.: Condens. Matter* **28**, 224005 (2016).